

Simulated evolution of the dark matter large-scale structure

M. Demiański^{1,2}, A. Doroshkevich³, S. Pilipenko³, S. Gottlöber⁴

¹*Institute of Theoretical Physics, University of Warsaw, 00-681 Warsaw, Poland*

²*Department of Astronomy, Williams College, Williamstown, MA 01267, USA*

³*Astro Space Center of Lebedev Physical Institute of Russian Academy of Sciences, 117997 Moscow, Russia*

⁴*Astrophysical Institute Potsdam, An der Sternwarte 16, 14482 Potsdam, Germany*

Accepted 25.11.06, Received ..., in original form ...

ABSTRACT

We analyze evolution of the basic properties of simulated large scale structure elements formed by dark matter (DM LSS) and confront it with the observed evolution of the Lyman- α forest. In three high resolution simulations we selected samples of compact DM clouds of moderate overdensity. Clouds are selected at redshifts $0 \leq z \leq 3$ with the Minimal Spanning Tree (MST) technique. The main properties of so selected clouds are analyzed in 3D space and with the core sampling approach, what allows us to compare estimates of the DM LSS evolution obtained with two different techniques and to clarify some important aspects of the LSS evolution. In both cases we find that regular redshift variations of the mean characteristics of the DM LSS are accompanied only by small variations of their PDFs, what indicates the self similar character of the DM LSS evolution. The high degree of relaxation of DM particles compressed within the LSS is found along the shortest principal axis of clouds. We see that the internal structure of selected clouds depends upon the mass resolution and scale of perturbations achieved in simulations. It is found that the low mass tail of the PDFs of the LSS characteristics depends upon the procedure of clouds selection.

Key words: cosmology: large-scale structure of the Universe — simulations: quasars: absorption: general — surveys.

1 INTRODUCTION

At $z \leq 1.5$ the Large Scale Structure of the Universe (LSS) is observed in many galaxy catalogs such as 2dFGRS, SDSS, DEEP2, VIRMOS (Percival et al. 2001; Verde et al. 2003; Abazajian et al. 2003; Davis et al. 2003; Le Fevre et al. 2005). It is manifested as a strong galaxy concentration within rich walls and filaments surrounding regions with low density of galaxies (voids). At redshifts $z \geq 2$ the LSS is observed as the Ly- α forest and rare metal systems in high resolution spectra of the farthest quasars. The observed properties of these populations of the LSS elements are different but now it is commonly believed that both of them represent *different manifestations* of the same structure formed by DM and baryonic components. This statement suggests that the Ly- α absorbers can be associated with low mass structure elements formed by the non luminous baryonic and DM components, while galactic walls and filaments represent fraction of the richer LSS elements. This means that the DM structure traced by the Ly- α absorbers is qualitatively similar to the rescaled structure observed in the spatial distribution of

galaxies. In particular, this inference is consistent with observations of absorbers in the vicinity of galactic filaments and even galaxies within voids (Morris et al. 1993a, b; Pentton, Stock and Shull 2000, 2002; McLin et al. 2002; Williger et al. 2010).

The facilities of both observational approaches are limited but they are complementary to each other. Thus analysis of the galaxy surveys is focused on the richer LSS elements at limited range of redshifts $z \leq 1 - 1.5$. It allows us to determine the main characteristics of such elements (see, e.g., Doroshkevich et al. 2004) but cannot trace the LSS evolution for large redshift intervals. This analysis is concentrated on the investigations of galactic properties and their environmental dependence. For example, it allows us to test the star formation histories (see, e.g., Panter et al. 2007; Skibba et al. 2009) and correlations between orientations of the LSS elements and the angular momentum of galaxies (see, e.g., Trujillo et al. 2006; Aragon-Calvo et al. 2007; Paz et al. 2008; Slozar et al. 2009; Jimenez 2009).

On the other hand, observations of the Ly- α forest at $z \sim 2 - 4$ allow us to trace some characteristics of the low

mass LSS elements and their evolution. However, they rely on the observed evolution of neutral hydrogen, which can be caused by many factors. Thus, in addition to the actual evolution of the DM components of the Ly- α absorbers the observed fraction of neutral hydrogen depends upon poorly known variations of the UV background. In spite of this, it is clear that there is a close link between the observed Ly- α absorbers and DM clouds formed at high redshifts.

It seems that the close link between the Ly- α forest and the galaxy LSS can be established by numerical simulations of the structure evolution. However, it is not yet possible to simulate the LSS evolution in a wide range of scales. Thus, simulations performed within large boxes with a moderate spatial and mass resolution (for review see Frenk 2002; Springel, Frenk & White 2006) reproduce reliably only the formation of the richer DM LSS elements similar to those observed in the galaxy distribution. On the other hand, high resolution simulations performed with the small box sizes can reproduce some characteristics of the Ly- α forest (see, e.g., Weinberg et al. 1998; Zhang et al. 1998; Davé et al. 1999; Theuns et al. 1999, 2000; Schaye 2001; Meiksin, Bryan and Machacek 2001) but obviously they cannot simulate formation of the richer LSS elements. Perhaps, more progress can be achieved with simulations performed with variable resolution (see, e.g., Springel et al. 2008; Diemand et al. 2008).

Technical limitations of the box size and resolution lead to small and large scale cutoffs of the simulated power spectrum. These cutoffs restrict the potential of such simulations and do not allow to reproduce reasonably well the observed characteristics of the Ly- α forest (see, e.g., Meiksin, Bryan and Machacek 2001; Gnedin & Hamilton 2002; Tegmark & Zaldarriaga 2003; Seljak, McDonald & Makarov 2003; Manning 2003a,b; Demiański & Doroshkevich 2003). Now such simulations are used mostly for the surprisingly stable reconstruction of the small scale initial power spectrum from characteristics of the forest (see, e.g., Croft et al. 2001, 2002; Seljak et al. 2005; McDonald et al. 2005; Viel et al 2004a, b).

An alternative approach is to focus the main attention on the regular trends in the evolution of the simulated LSS and compare them with observations of the forest properties in a wide range of redshifts. Such trends can be revealed with special methods applied to representative high resolution simulations. The successful investigation of the process of halo formation (see, e.g., Navarro, Frenk, & White, 1995, 1996, 1997; Bullock et al., 2001; Tasitsiomi et al. 2004) demonstrates the high potential of this approach.

The statistical analysis of a large sample of the Ly- α absorbers (Demiański, Doroshkevich & Turchaninov 2006; Demiański & Doroshkevich 2010) reveals some unexpected features of the forest evolution. The most important are the regular redshift variations of the mean observed characteristics of the Ly- α absorbers and the surprisingly weak variations of their probability distribution functions (PDFs). These results demonstrate the self similar character of evolution of the observed LSS, which must be tested with numerical simulations.

Other important open problems are connected with the internal structure of the Ly- α absorbers and its evolution with time. They also include an estimate of the degree of relaxation of matter accumulated by absorbers with various

richness, and the link between the thermal and large scale bulk motions of the gas and the observed Doppler parameters of the forest. At the present time a reliable observational discrimination between contributions of these factors is problematic. We can also note the surprisingly weak redshift evolution of the observed mean Doppler parameter and a complex shape of its PDF indicating the existence of a rich sample of DM clouds with small Doppler parameter $b \leq \langle b \rangle$.

Comparison of the observed evolution of the forest with the simulated evolution of the DM clouds allows us to clarify how they are related. For this purpose, in this paper, we investigate evolution of the DM LSS in high resolution simulations using the Minimal Spanning Tree (MST) and Core Sampling approaches (see, e.g., Doroshkevich et al. 2004). The space and force resolutions achieved in these simulations allow us to characterize the evolution of the compact DM LSS elements with moderate richness, which is by itself an important problem. Thus, we reveal significant differences in properties and evolution rates of the LSS elements selected in simulations with different mass and space resolutions. These results demonstrate the strong influence of small scale perturbations on the internal structure of the LSS elements.

All selected DM elements are significantly larger than those observed as the Ly- α forest, what does not allow us to perform a direct quantitative comparison of the observed and simulated clouds. However, the basic properties of the selected sample of DM clouds are found to be similar to the properties of the observed Ly- α forest. In particular, we confirm the self similar character of evolution of the DM LSS, reproduce the redshift dependence and the PDF of the Doppler parameter, estimate the clouds rotation, the contribution of macroscopic turbulent motions and the degree of relaxation of compressed matter measured along the principal axes of clouds. The properties of the LSS elements are found to be qualitatively consistent with predictions of the Zel'dovich approximation (Zel'dovich 1970; Shandarin & Zel'dovich 1989; Demiański & Doroshkevich 1999, 2004).

This paper is organized as follows. Simulations that we use and methods of their analysis are shortly presented in Sec. 2. Evolution of the basic characteristics of the DM LSS is described in Sec. 3 and results of the core sampling analysis are given in Sec. 4. Discussion of obtained results and conclusions can be found in Sec. 5.

2 NUMERICAL SIMULATIONS

In this paper we investigate the process of formation and evolution of the DM LSS within the concordance cosmological model

$$\Omega_{\Lambda} = 0.7, \quad \Omega_m = 0.3, \quad h = 0.7, \quad \sigma_8 = 0.9, \quad n = 1,$$

where Ω_{Λ} and Ω_m denote the dimensionless densities of Dark Energy and matter, $h = H_0/100 \text{ km/s/Mpc}$ the dimensionless Hubble parameter, σ_8 - the amplitude of density perturbations, n - the power index of the spectrum of perturbations.

One simulation - referred further as S_{150} - was performed with an MPI version of the Adaptive Refinement Tree code (Kravtsov et al. 1997) within a box of $L_{box} = 150h^{-1} \text{ Mpc}$ with 256^3 particles, cell size $\approx 0.6h^{-1} \text{ Mpc}$ and

mass and force resolutions of $1.7 \cdot 10^{10} h^{-1} M_{\odot}$ and $18 h^{-1} \text{kpc}$ (see Wojtak et al., 2005 for more details). We have analyzed the simulated DM distribution at four redshifts, namely, at $z = 0, 1, 2$ & 3 , what roughly covers the interval of observed redshifts.

For comparison we also used the DM distribution obtained in the MareNostrum Universe (Gottlöber, Yepes 2007). This non-radiative SPH simulation was performed with GADGET2 code (Springel 2005) using the concordance model. This simulation - further referred as S_{500} - consists of 1024^3 dark and 1024^3 gas particles in a box of $L_{box} = 500 h^{-1} \text{Mpc}$ on a side. Both the mass and force resolutions ($0.75 \cdot 10^{10} h^{-1} M_{\odot}$, $15 h^{-1}$ comoving kpc) are comparable to those achieved in the previous simulation. Such comparison allows us to check the impact of the baryonic component, the code used and the initial realization on the properties of the simulated LSS. As a rule, properties of clouds selected in this simulation are close to the ones obtained for the simulation S_{150} , what demonstrates the weak impact of these factors on the characteristics of the LSS.

The third simulation - further referred as S_{50} - consists of 512^3 DM particles in a box of $L_{box} = 50 h^{-1} \text{Mpc}$ on a side. It was performed at the Astrophysical Institute Potsdam by M. Steinmetz. With such parameters the obtained mass resolution is $7.8 \cdot 10^7 h^{-1} M_{\odot}$ and the force resolution $3 h^{-1}$ comoving kpc, which is better than resolutions achieved in the previous simulations. However, in this case the important influence of large scale perturbations is partly suppressed. Comparison of results obtained for these three simulations reveals the impact of small scale perturbations on the properties of the LSS. In particular, in this simulation we see more complex internal structure of the selected LSS elements, earlier formation of high density clouds, and we can trace the initial steps of the LSS formation up to redshifts $z \sim 12 - 14$.

2.1 Selection of high density clouds

Using the Minimal Spanning Tree (MST) code as described in Doroshkevich et al. (2004) we select from the full distribution of DM particles a set of clouds with three threshold parameters that restrict their density and richness. They are the threshold overdensity, δ_{thr} , and the minimal and maximal richness, N_{min} & N_{max} , of selected clouds

$$\delta_{thr} = (4\pi \ell_{thr}^3 \langle n_p \rangle / 3)^{-1}, \quad N_{min} \leq N_p \leq N_{max}, \quad (1)$$

$$\langle n_p \rangle = (5, 8.6 \text{ \& } 10^3) h^3 \text{Mpc}^{-3}, \quad \langle \rho \rangle \approx 8 \cdot 10^{10} h^2 M_{\odot} / \text{Mpc}^3.$$

Here ℓ_{thr} is the maximal length of the edges of the tree within a selected cloud, $\langle \rho \rangle$ and $\langle n_p \rangle$ are the mean comoving density and number density of DM particles in the simulations. Using these parameters we can reliably identify clouds even of a complex irregular shape. By definition of the MST the distances between all neighboring points inside the cloud are less than the threshold one, $\ell \leq \ell_{thr}$, and, therefore, $\delta = \rho / \langle \rho \rangle \geq \delta_{thr}$. In other words, the selected clouds are bound by the surfaces of constant overdensity, $\delta = \delta_{thr}$.

In this paper we are mainly interested in the mildly nonlinear evolution of the LSS elements with moderate overdensity. Such elements dominate at the early period of the LSS formation and it can be expected that we observe them as the Ly- α forest. Hence the threshold overdensities that

we adopt in this paper are not very high: $\delta_{thr} = 1$ and $\delta_{thr} = 1.76$.

The other important threshold parameters are the minimal and maximal richness of the selected clouds. The first one ensures the reliability and stability of characteristics of the selected clouds, while the second one allows us to exclude from the analysis amorphous multiconnected clouds formed at later stages of the LSS evolution. Such extremely rich clouds appear owing to the integration of less rich clouds and they represent the elements of the well known network of the LSS. Evidently, such clouds can not be described by just a few local characteristics.

For these simulations we use the following minimal and maximal richness of the clouds under investigation

$$\begin{aligned} N_{min} &= 30, & N_{max} &= 5000, & \text{for } S_{150}, \\ N_{min} &= 70, & N_{max} &= 11\,000, & \text{for } S_{500}, \\ N_{min} &= 6.5 \cdot 10^3, & N_{max} &= 10^6 & \text{for } S_{50}, \end{aligned} \quad (2)$$

what approximately corresponds to the same range of cloud masses,

$$M_{min} \simeq 5 \cdot 10^{11} h^{-1} M_{\odot}, \quad M_{max} \simeq 8 \cdot 10^{13} h^{-1} M_{\odot}. \quad (3)$$

Further on we refer to the samples selected with $M_{min} \leq M_{cl} \leq M_{max}$ as samples of compact clouds. For some tests we also use samples with $M_{cl} > M_{min}$ (a full sample) and $M_{cl} > M_{max}$ (a sample of rich clouds).

The selection of clouds with the core sampling approach is described in Sec. 4.

2.2 Characteristics of clouds

In this paper clouds are characterized by their principal axes determined by their inertia tensor. Such rough description allows us to take into account the main global shape of the clouds and to estimate their degree of filamentarity and sheetness without introduction of any additional parameters.

Sometimes much more refined techniques are used for selection and discrimination of the DM filaments and walls (see, e.g., discussion in Doroshkevich et al. 2004; Aragon-Calvo et al. 2007; Zhang et al. 2009). However, advantages of such approach are problematic owing to very complex shapes, many branches and strong nonhomogeneity of the matter distribution typical for both the observed and simulated LSS elements. In contrast to our approach such refined methods are inevitably multiparametric and therefore description of so selected clouds becomes more complicated. Such approach can be efficient in providing more accurate description of local environment of considered objects.

Here we consider several global characteristics of clouds, namely, their mass (richness) and velocity, M_{cl} & \mathbf{U} , three components of their angular momenta J_i and the comoving sizes along the three principal axes, $L_1 \geq L_2 \geq L_3$, determined through their inertia tensors.

As is well known (see, e.g., review by Schäfer 2008) the angular momenta of the clouds are mainly generated by the tidal interactions with the surrounding medium (Tidal Torque Theory (TTT) Peebles 1969; Doroshkevich 1970; White 1984). The angular momentum of a cloud depends upon its (random) shape. The mean angular momentum of

clouds is small, $\langle J_i \rangle \sim 0$ owing to its random orientation and $\langle J_i^2 \rangle$ provides more stable characteristics of clouds. For a regular ellipsoidal volume with halfaxes $a_1 \geq a_2 \geq a_3$, the Zel'dovich theory gives

$$\langle J_i \rangle = 0, \quad \langle J_i^2 \rangle \propto (a_j^2 - a_k^2)^2, \quad i \neq j \neq k, \quad (4)$$

and, so, $\langle J_2^2 \rangle \geq \langle J_{1,3}^2 \rangle$ (Demiański & Doroshkevich 2004).

In simulations the angular momenta of clouds and the contribution of bulk (turbulent) motions are characterized by the functions

$$J_i = N_p^{-1} \sum_{m=1}^{N_p} \psi_i, \quad \psi_i = \epsilon_{ikl} (\mathbf{v}_m - \mathbf{v}_c)_k (\mathbf{x}_m - \mathbf{x}_c)_l, \quad (5)$$

where ϵ_{ikl} is the totally antisymmetric unit tensor and N_p is the number of particles in the cloud. Here \mathbf{x}_m & \mathbf{v}_m and \mathbf{x}_c & \mathbf{v}_c are the coordinates and velocities of the m^{th} particle and the center of mass, respectively.

To characterize the internal dynamics of matter accumulated by a cloud and its degree of relaxation along the principal axes we consider also three velocity dispersions, σ_i , and three angular momenta of particles, j_i ,

$$j_i = N_p^{-1} \sum_{m=1}^{N_p} |\psi_i|. \quad (6)$$

For a regular ellipsoidal volume with halfaxes $a_1 \geq a_2 \geq a_3$, the Zel'dovich theory gives in contrast to (4)

$$\langle j_i^2 \rangle \propto (a_k^2 + a_l^2)^2, \quad i \neq k \neq l. \quad (7)$$

As is well known, within anisotropic clouds of collisionless particles the relaxation occurs independently along each principal axis of the cloud. For example, the observed galactic walls and filaments are almost relaxed along their shortest axes but have no time to relax along their longest axis. Thus, here we will characterize the degree of relaxation of N_p particles compressed within a cloud by the parameters

$$w_i = 1 + \frac{1}{N_p \sigma_i} \sum_{m=1}^{N_p} (\mathbf{v}_m - \mathbf{v}_c)_i (\mathbf{x}_m - \mathbf{x}_c)_i / |(\mathbf{x}_m - \mathbf{x}_c)_i|. \quad (8)$$

Here σ_i is the velocity dispersion and index i shows that we consider the relaxation along the i^{th} principal axis.

Evidently, the functions w_i discriminate between contributions of random and regular motions. Indeed, for a cloud with relaxed matter distribution and random velocities of particles we can expect that $|w_i - 1| \ll 1$, because for each particle the probabilities to find $(\mathbf{v}_m - \mathbf{v}_c)(\mathbf{x}_m - \mathbf{x}_c)_i \leq 0$ and $(\mathbf{v}_m - \mathbf{v}_c)(\mathbf{x}_m - \mathbf{x}_c)_i \geq 0$ are close to each other. In contrast, for regular expansion or compression of matter $(\mathbf{v}_m - \mathbf{v}_c)$ and $(\mathbf{x}_m - \mathbf{x}_c)$ are correlated and, so, $|w_i - 1| \sim 1$ seems to be much more probable. The case when $w_i \geq 1$ or $w_i \leq 1$ corresponds to domination of the expansion or compression of matter along the i^{th} axis.

The core sampling approach was applied only for the first simulation and is described in Sec. 4.

2.3 Comparison of the simulations with the Zel'dovich approximation

In this paper we consider properties of DM clouds selected in the same manner in three simulation. The simulations

are performed with different codes, in different boxes and with different resolution. The cloud selection is performed with a complex algorithm and with set of thresholds presented in Sec. 2.1. Therefore before we start our analysis we estimate the representativity and reliability of the samples of selected clouds. For this purpose we compare some integral characteristics of selected clouds with predictions of the Zel'dovich approximation (Zel'dovich 1970; Shandarin & Zel'dovich 1989; Demiański & Doroshkevich 1999, 2004), which reliably describes the mildly nonlinear evolution of perturbations.

For this aim we use here three characteristics of samples of clouds, namely, the matter fraction accumulated by the LSS, $f(M)$, the PDFs of masses of selected clouds, $P(M)$, and the redshift evolution of the velocity of clouds as a whole, $\mathbf{U}(z)$. The last test is more sensitive to the large scale perturbations, while the first and the second ones are sensitive to the small scale perturbations, nonlinear processes of matter condensation within clouds and the procedure of clouds selection.

The shape of PDFs for clouds sizes and internal velocities can be also obtained on the basis of Zel'dovich theory. However, here we note only that for these functions and the CDM-like power spectrum the Gaussian PDF of initial perturbations is transformed to the exponential one (see sections 2.4 & 3.3 in Demiański & Doroshkevich (2004) for more details). The exponential shape of these PDFs in our simulations is clearly seen in Figs 1 and 2. In Sec. 3.3 we compare predictions of the Zel'dovich theory with the simulated angular momentum and turbulent motions (4, 7).

2.3.1 Evolution of the cloud velocity

The nonlinear processes of matter clustering and relaxation of the compressed matter strongly distort velocities of particles within clouds but only weakly change the velocities of clouds as a whole. As noted in Demiański & Doroshkevich (1999), for the Gaussian initial perturbations, the PDF of clouds velocity remains Gaussian with the velocity dispersion closely allied to that described by the linear theory. Thus, according to the Zel'dovich approximation the velocity dispersion along any principal direction is

$$\sigma_U = \frac{H(z)}{1+z} \beta(z) B(z) \frac{\sigma_s}{\sqrt{3}}, \quad \beta(z) = -\frac{1+z}{B(z)} \frac{dB(z)}{dz}, \quad (9)$$

$$B^{-3} \approx 1 + \frac{2.2\Omega_m}{1+1.2\Omega_m} [(1+z)^3 - 1],$$

$$H^2 = H_0^2 (\Omega_m (1+z)^3 + \Omega_\Lambda), \quad \sigma_s^2 = \frac{1}{2\pi} \int_0^\infty p(k) dk.$$

Here H is the Hubble parameter, $H_0 = 100 \text{ h km/s/Mpc}$, $B(z)$ describes the growth of perturbations in the linear theory for Λ CDM cosmology, $p(k)$ and $H(z)\sigma_s$ are the power spectrum and the amplitude of initial velocity perturbations, Ω_m and Ω_Λ are matter and Dark Energy density parameters. For both our simulations with the moderate resolution we have approximately

$$\sigma_s \approx \frac{2.07}{\Omega_m h^2} \sigma_8 \text{ Mpc}, \quad B \approx 1.27 [1 + (1+z)^3]^{-1/3},$$

and for $z \geq 1$ we get

$$H(z) \approx H_0 \sqrt{\Omega_m} (1+z)^{3/2}, \quad B(z) \approx 1.27 (1+z)^{-1},$$

$$\sigma_U \approx 353 \text{ km/s} (1+z)^{-1/2} (\sigma_8/0.9). \quad (10)$$

Using the matter velocities in the simulation S_{150} we get for the 1D velocity dispersion of clouds at $z \geq 1$

$$\sigma_U = 325 \text{ km/s} (1+z)^{-1/2} (1 \pm 0.04), \quad (11)$$

and for the high resolution simulation S_{50} we get

$$\sigma_U = 315 \text{ km/s} (1+z)^{-1/2} (1 \pm 0.04). \quad (12)$$

The differences ($\sim 8\%$ & 11%) between the expected (10) and simulated (11, 12) dispersions characterize the impact of the large scale perturbations suppressed in simulations owing to the finite box size.

For clouds selected in the simulation S_{150} with the threshold overdensity $\delta_{thr} = 1.76$ and richness $3 \cdot 10^{12} h M_\odot \leq M_{cl} \leq 5 \cdot 10^{14} h M_\odot$ at redshifts $z = 1, 2 \& 3$ the probability distribution function (PDFs) for the cloud velocities, $P_U(|U_j|/\sigma_U)$, $j = 1, 2, 3$ are similar to each other with high precision and are well fitted by the function

$$P_U(x_j) = 0.77 \exp(-x_j^2/2), \quad x_j = |U_j|/\sigma_U. \quad (13)$$

Small variations around the Gaussian fit (13) depend on peculiarities of the selected sample of clouds and can also indicate the weak mass dependence of the measured dispersions.

2.3.2 The matter fraction accumulated by the LSS

To test the simulations and our clouds selection algorithm we compare the expected and measured matter fraction accumulated by the LSS. According to the Zel'dovich theory the fraction of matter expanding along all three axes is $f_{exp} \approx 0.5^3 = 0.125$ and, therefore, the fraction of matter accumulated by all LSS elements is

$$f_{tot} \approx 0.875(1 - z/z_f), \quad z \ll z_f. \quad (14)$$

This approximate relation slightly overestimates the total mass accumulated by pancakes, filaments and clouds. More accurate but multiparametric and more complex estimates can be found in Demiański & Doroshkevich (1999, 2004).

For the simulation S_{150} we get for $\delta_{thr} = 1$ at $z \leq 3$

$$f(M \geq 5 \cdot 10^{11} h^{-1} M_\odot) \approx 0.73(1 - z/5.7). \quad (15)$$

For the high resolution simulation S_{50} we see earlier matter concentration and for $\delta_{thr} = 1$, at $z \leq 6$, we get

$$f(M \geq 2.5 \cdot 10^9 h^{-1} M_\odot) \approx 0.80(1 - z/10), \quad (16)$$

$$f(M \geq 5 \cdot 10^{11} h^{-1} M_\odot) \approx 0.67(1 - z/10).$$

The moderate differences between the measured (15, 16) and expected (14) values demonstrate the moderate impact of the used selection parameters used, mostly the minimal mass. The earlier matter condensation in the high resolution simulation S_{50} (16) as compared with the simulation S_{150} (15) illustrates the impact of the small scale perturbations represented by the power spectrum of simulation S_{50} .

2.3.3 The mass function of clouds

For high density virialized DM clouds the Press-Schechter mass distribution is usually reproduced in simulations. However, we will see below that for strongly anisotropic partly

relaxed clouds selected with moderate overdensity the simulated mass functions are well approximated by a power law. Simple qualitative explanation of such distribution is offered by the Zel'dovich theory.

According to this theory the process of the compact object formation is determined by three conditions

$$\Delta q_i - B(z)\Delta S_i = 0, \quad i = 1, 2, 3,$$

where the function $B(z) \leq 1$ was introduced in (9) and ΔS_i are the relative displacements of two points separated by the comoving distance Δq_i along i^{th} principal direction. This means that the expected collapsed volume, V_q , and corresponding mass, M_{zt} , can be qualitatively estimated as

$$M_{zt} \propto V_q = \Delta q_1 \Delta q_2 \Delta q_3 \propto V_s = \Delta S_1 \Delta S_2 \Delta S_3, \quad (17)$$

$$\Delta S_i > q_{min} \geq 0.$$

Here this condition assures that the collapse proceeds along all three directions and restricts the volume V_s .

For any M_0 the probability to find the mass of collapsed clouds in the range $M_0 - \Delta M \leq M_{zt} \leq M_0 + \Delta M$ is proportional to the probability to find $\Delta S_i \geq q_{min} \geq 0$, and the volume V_s in corresponding range $V_0 - \Delta V \leq V_s \leq V_0 + \Delta V$. This simple approach allows us to characterize the shape of the PDF $P(V_s) \propto P(M_{zt})$ but its normalization (in 17) requires additional assumptions. More detailed description of the complicated process of clouds formation inevitably leads to much more complex multiparametric expressions (see, e.g., Demiański & Doroshkevich 2004).

In turn, the PDF $P(V_s)$ can be directly obtained from the PDF $P(\Delta S_i)$. For this purpose we use the simple three step numerical method: 1. to construct the 3D sample of ΔS_i in accordance with the theoretical PDF $P(\Delta S_i)$; 2. to select 1D subsample of V_s in accordance with the conditions (17); 3. to construct the PDF $P(V_s)$.

The PDF $P(\Delta S_i)$ is Gaussian (Demiański & Doroshkevich 1999, 2004) with dispersion $\sigma_S(\Delta q)$ and weak correlations,

$$\xi_{ik} = \langle \Delta S_i \Delta S_k \rangle / \sigma_S^2 \leq 1/3, \quad i \neq k.$$

With this PDF we constructed 10^6 realizations of ΔS_i and found that the PDF $P(V_s)$ can be fitted by a power law $P(V_s) \propto V_s^\kappa$. The slope κ slightly varies depending on the considered range of $V_s \geq V_{min}$. Thus, for three progressively decreasing $V_{min} = V_1, 0.1V_1, \& 0.01V_1$ the selected subsamples contain 30 407, 50 025 and 164 103 elements with the slope of PDFs $\kappa \sim -2.5, -1.8 \& -1.5$, respectively. These variations indicate that this slope increases for larger V_s .

In all simulations considered below the PDFs of masses of selected clouds are fitted by power laws with $\kappa = -2, -2.4, -2.2$ (19, 20, 22) what is in the range of expected values $-1.8 \geq \kappa \geq -2.5$. These variations of κ indicate mainly the impact of the resolution achieved in simulations and the range of selected masses.

3 PROPERTIES OF SIMULATED DM LSS

As is well known formation of the LSS begins at high redshifts and its evolution continues up to now. The matter fraction accumulated within the LSS elements increases with time owing to both the accretion of matter on the earlier

formed LSS elements and creation of new low mass LSS elements and bridges leading to the successive integration of the LSS elements into multiconnected richer ones. At small redshifts these processes lead to the creation of the joint network of compressed matter. The high efficiency of clouds integration demonstrates the correlated character of the LSS formation and the interaction of small and large scale perturbations. Here we present some quantitative characteristics of these processes obtained for the LSS formed by the DM particles only.

In some important aspects these clouds differ from the LSS formed by both the DM and baryonic components and observed as the Ly- α forest. In turn, both these structures differ from the LSS formed by the luminous matter (galaxies) and observed in large galactic surveys. None the less, all these LSS elements are dominated by the DM component and their evolution is driven by the same initial perturbations. So, it can be expected that the most fundamental properties of the LSS evolution can be established through the analysis of the simulated DM LSS.

In this section we consider the clouds selected with the threshold overdensity, $\delta_{thr} = 1.76$, what allows us to partly suppress formation of the very massive multiconnected clouds at redshifts $z \leq 2$. Further on we will present results obtained for the sample of compact LSS elements with DM masses $10^{12} M_{\odot} \leq M \leq 5 \cdot 10^{14} M_{\odot}$.

For the high resolution simulation S_{50} we can obtain more detailed description of the process of matter condensation within various samples of high density clouds. Thus, we have found that within the LSS clouds there is a population of high density cores with $\delta \geq 10$. Such early formation of high density low mass clouds was found also by Diemand et al. (2008).

3.1 Basic characteristics of compact clouds

The set of selected compact clouds can be characterized by the redshift evolution of their comoving number density, $\langle n_{cls}(z) \rangle$, masses, $\langle M_{cl}(z) \rangle$, the fraction of particles accumulated by clouds, f_{com} , and three comoving sizes $\langle L_i(z) \rangle$ ($i = 1, 2, 3$) determined along the three principal axes of each cloud.

For the sample of $N_{cls} \sim 11\,000 - 14\,000$ clouds selected in the simulation S_{150} with $\delta_{thr} = 1.76$ and $M_{min} \leq M_{cl} \leq M_{max}$, we have with variations smaller than 10%:

$$\langle n_{cls}(z) \rangle \approx 3.6 \cdot 10^{-3} \text{Mpc}^{-3}, \quad \langle M_{cl}(z) \rangle \approx 3 \cdot 10^{12} h^{-1} M_{\odot},$$

$$f_{com} = \langle n_{cls} \rangle \langle M_{cl} \rangle / \langle \rho \rangle \approx 0.13,$$

$$\langle L_i(z) \rangle \approx \ell_i \sqrt{\nu}, \quad \nu = M_{cl} / \langle M_{cl}(z) \rangle, \quad (18)$$

where ℓ_i are reduced cloud sizes with

$$\langle \ell_1 \rangle = 1 h^{-1} \text{Mpc}, \quad \langle \ell_2 \rangle = 0.5 h^{-1} \text{Mpc}, \quad \langle \ell_3 \rangle = 0.2 h^{-1} \text{Mpc}.$$

All these parameters characterize the selected sample of the LSS elements. Mass dependence of the cloud sizes reflects the complex structure of selected clouds and implies their partial correlation. Their weak dependence on redshift characterizes the balance between creation of new elements and matter outflow to the more massive complex LSS elements caused by creations of bridges between earlier formed clouds.

The PDFs of the functions ℓ_i plotted in Fig. 1 are also

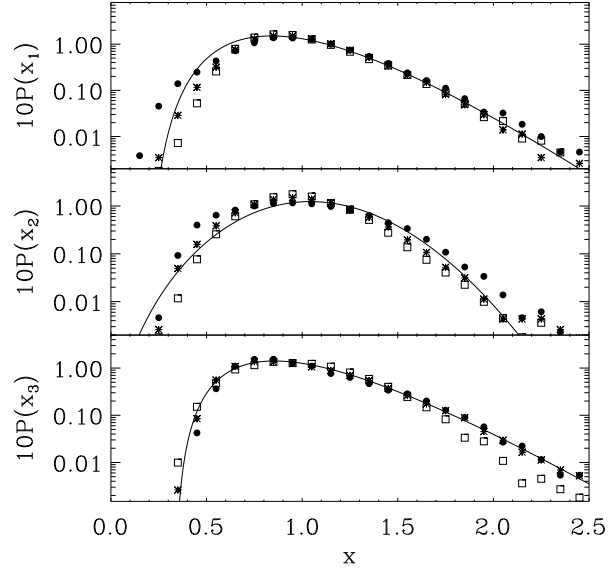


Figure 1. The PDFs of clouds sizes ℓ_i along the longest, middle, and shortest principal axes (top, middle and bottom panels) are plotted for redshifts $z = 1, 2 \& 3$ (points, stars and squares) for clouds selected in simulation S_{150} with the threshold overdensity $\delta = 1.76$ and richness given by (3). Here $x_i = \ell_i / \langle \ell_i \rangle$.

weakly dependent upon redshift. The exponential decline of the PDFs at $x_i = \ell_i / \langle \ell_i \rangle \geq 1$ reflects the rare formation of asymmetric objects with large ℓ_i while at $x_i \leq 1$ the shape of the PDFs depends upon conditions used for the cloud selection.

The PDF of cloud masses, $P_p(M_{cl} / \langle M_{cl} \rangle)$, is surprisingly independent from redshift but depends upon the range of considered velocity dispersion of compressed matter (see Sec. 3.5). For all clouds it can be approximated by the power law

$$P_p(\nu) = 0.25 \nu^{-2}, \quad \nu = M_{cl} / \langle M_{cl} \rangle, \quad (19)$$

what is close to predictions of the Zel'dovich theory (sec. 2.3.3). It is interesting that here we do not see the exponential decline of the PDF, $P_p(x)$, predicted by all theoretical models and observed in the luminosity function of galaxies. In the simulations such decline appears only at higher redshifts for clouds selected with larger threshold overdensity. It can be expected that these differences reflect the complex structure of richer clouds formed partly by integration of earlier formed clouds due to origin of low density bridges between them.

Let us note again that both the mean values $\langle L_i \rangle$ and PDFs for the cloud sizes, $P(x_i = \ell_i / \langle \ell_i \rangle)$, plotted in Fig. 1 do not change with redshift. These results show that for so selected clouds, their mean sizes in real space increase with time $\propto (1+z)^{-1}$ along each of the three principal axes. This means that the mean cloud overdensity does not change and, therefore, the possible dissipation of the LSS elements owing to the matter expansion is not so essential.

The characteristics of compact clouds obtained in the simulation S_{500} are quite similar to those presented above. Let us only note that for this simulation we find some excess of low mass clouds as compared with the simulation S_{150} .

Indeed, instead of (19) we get for this simulation the PDF

$$P_p(\nu) \propto \nu^{-2.4}, \quad \nu = M_{cl}/\langle M_{cl} \rangle, \quad (20)$$

what confirms some excess of less massive clouds. This PDF differs from (19) but it is in the range of predictions of the Zel'dovich theory (sec. 2.3.3) and is quite similar to that obtained below for colder less massive clouds (35). This difference shows that some properties of the selected clouds are sensitive to such factors as the possible impact of the gaseous component, the initial realization of perturbations, and the criteria of the clouds selection.

Analysis of the high resolution simulation S_{50} allows us to obtain more detailed description of the evolution of compact clouds. As was noted above in this simulation we see formation of the rich population of high density cores with the overdensity $\delta_{thr} \geq 10$ and $M_{cl} \geq 10^{10} M_\odot$. These cores have steep density profiles $\rho \propto r^{-2}$ and accumulate up to 40% of matter at $z = 1$. They are usually incorporated into less dense clouds.

For the selected LSS elements we can trace their evolution in a wider range of redshifts, $1 \leq z \leq 6$. Thus, instead of (18) we get

$$\langle n_{cls}(z) \rangle \approx 6.3 \cdot 10^{-3} (1 - 0.1z) \text{Mpc}^{-3},$$

$$\langle M(z) \rangle \approx 2.3 \cdot 10^{12} (1 - 0.07z) h^{-1} M_\odot,$$

$$f_{com} \approx 0.18 (1 - 0.16z),$$

$$L_i = \ell_i \sqrt{\nu}, \quad \nu = M_{cl}/\langle M_{cl}(z) \rangle, \quad (21)$$

$$\langle \ell_1 \rangle = 0.65 (1 + 0.25z) h^{-1} \text{Mpc},$$

$$\langle \ell_2 \rangle = 0.2 (1 + 0.5z) h^{-1} \text{Mpc},$$

$$\langle \ell_3 \rangle = 0.1 (1 + 0.5z) h^{-1} \text{Mpc}.$$

At $z = 3$ these sizes are quite similar to (18) but at all redshifts we see a slow continuous matter compression. This difference reflects both the impact of small scale perturbations and a more detailed description of the LSS evolution achieved in the high resolution simulation.

The PDFs for the cluster sizes and their masses are also similar to the previous ones. In particular,

$$P_p(\nu) \propto \begin{cases} \nu^{-2.0}, & z \leq 3, \\ \nu^{-2.2}, & z > 4, \end{cases} \quad \nu = M_{cl}/\langle M_{cl} \rangle, \quad (22)$$

what is also consistent with predictions of the Zel'dovich theory. For larger threshold overdensity the theoretically expected exponential decline of the mass function can be seen for high z , when majority of clouds are well separated. For the mass function of high density halos selected within this simulation the exponential decline is clearly seen at all redshifts.

3.2 The velocity dispersion of compressed matter

The velocity dispersion of particles within selected clouds depends on three factors, which are: the retained Hubble expansion, the enhanced random initial velocities of particles, and the velocity created in the course of matter relaxation. All these factors are closely linked with the clouds mass and therefore the measured velocity dispersion also depends upon mass. The relative contributions of these components vary with time but for collisionless DM particles the rate of

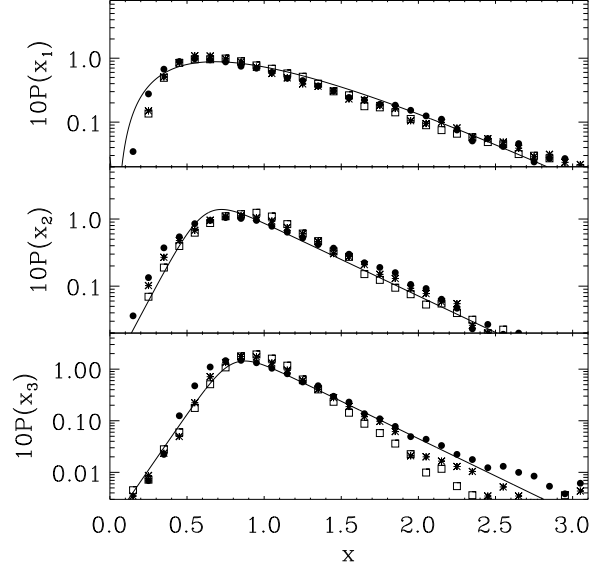


Figure 2. For the simulation S_{150} the PDFs of the reduced velocity dispersion, $c_{1,2,3}$, along the longest, middle and shortest principal axes (top, middle and bottom panels) are plotted for redshifts $z = 1, 2 \& 3$ (points, stars and squares) for clouds selected with the threshold overdensity $\delta = 1.76$ and richness given by (3). Here $x_k = c_k/\langle c_k \rangle$, $k = 1, 2, 3$.

these variations depends upon degree of matter compression and relaxation achieved along each of the principal axes. This means that the velocity dispersions along these axes are different and must be determined separately along the longest, σ_1 , middle, σ_2 , and shortest, σ_3 , principal axes of each cloud.

It is important that these velocity dispersions are much smaller than the dispersions σ_U introduced in (11). This difference is caused by the strong correlation of the particle velocities at the scales of clouds. The simple analysis shows that the dispersion of initial velocities within clouds decreases with the cloud mass, what stimulates the formation of low mass high density clouds.

For clouds selected in the simulation S_{150} with $\delta_{thr} = 1.76$ and $M_{min} \leq M_{cl} \leq M_{max}$ the velocity dispersions along three principal axes, σ_i , slowly vary with time but they depend upon the cloud richness,

$$\sigma_i = c_i \nu^{\alpha_i}, \quad \alpha_1 = 0.5, \quad \alpha_2 = 0.4, \quad \alpha_3 = 0.3. \quad (23)$$

The mean values of the reduced velocity dispersions c_i are

$$\langle c_1 \rangle = 58 \text{ km/s}, \quad \langle c_2 \rangle = 66 \text{ km/s}, \quad \langle c_3 \rangle = 80 \text{ km/s}, \quad (24)$$

and their PDFs, $P(x_i = c_i/\langle c_i \rangle)$, are plotted in Fig. 2 for three redshifts $z = 1, 2, 3$. The very weak redshift evolution of these PDFs verifies the self similar character of the simulated LSS evolution.

These PDFs demonstrate the expected exponential decline $P(x_i) \propto \exp(-x_i/0.3)$ for $x_i \geq 1$. At the same time, there are cold clouds with $c_i \leq \langle c_i \rangle$.

For the simulation S_{500} the velocity dispersions, $\langle c_i \rangle$ are $\sim 20\%$ smaller than (23). It is consistent with the excess of low mass clouds noted above (20) and confirms the sensitivity of the characteristics of the low mass clouds to the mass resolution, impact of the gaseous component and real-

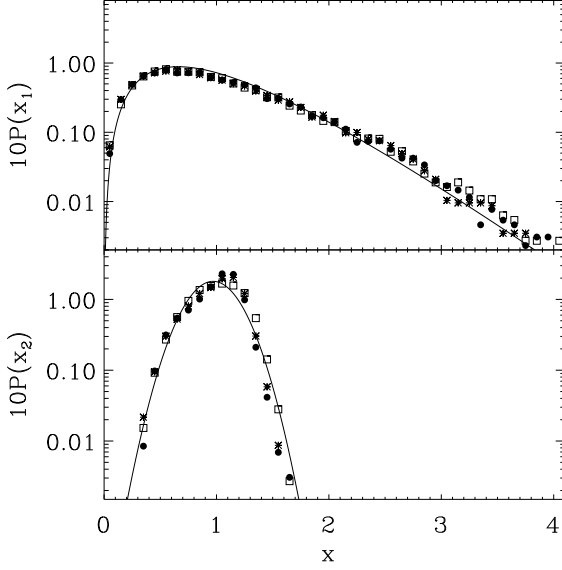


Figure 3. The PDFs of the reduced integral angular momentum, μ , and the reduced integral intensity of turbulent motions, τ , are plotted for redshifts $z = 1, 2$ & 3 (points, stars and squares) for clusters selected with the threshold overdensity $\delta = 1.76$ and richness given by (3). Here $x_1 = \mu/\langle\mu\rangle$, $x_2 = \tau/\langle\tau\rangle$.

ization of the initial velocity field. The PDFs of the velocity dispersions are also similar to those plotted in Fig. 2.

For the simulation S_{50} , for the same mass range, at redshifts $1 \leq z \leq 5$ the mean velocity dispersions are described by the relation (23) with

$$\alpha_1 = 0.4, \alpha_{2,3} = 0.3$$

$$\langle c_1 \rangle \approx 105(1 - 0.15z) \text{ km/s}, \quad (25)$$

$$\langle c_2 \rangle \approx 95 \text{ km/s}, \quad \langle c_3 \rangle \approx 80 \text{ km/s}.$$

Their PDFs are quite similar to those plotted in Fig. 2.

Differences between estimates (23, 24) and (25) can be related to the influence of small scale perturbations resulting in a more rapid relaxation and more complex internal structure of selected compact clouds. This is seen as the formation of high density cores within these clouds and as a decrease of power indices α_1 & $\alpha_{2,3}$ in (25) as compared with (23). In turn, action of these factors increases the reduced velocity dispersions c_1 & c_2 (25) as compared with (24). At the same time, for both simulations α_3 and c_3 remain quite similar.

3.3 Rotation and turbulent motions of the compressed matter

In the partly relaxed clouds particles move on closed orbits what generates both the turbulent motions, j_i (6) and the angular momenta of clouds as a whole, J_i (5) along three principal axes. Evidently, for isotropic simulations $\langle J_i \rangle = 0$ and further on we will consider characteristics of the absolute values of angular momenta $|J_i|$ only. As before, these functions depend upon cloud richness. For clouds selected in the simulation S_{150} we have

$$|J_i| = \mu_i g_i, \quad j_i = \tau_i g_i, \quad (26)$$

$$g_1^2 = (L_2^2 + L_3^2)(\sigma_2^2 + \sigma_3^2), \quad g_{2,3}^2 = (L_1^2 + L_{3,2}^2)(\sigma_1^2 + \sigma_{3,2}^2),$$

where μ_i & τ_i characterize dimensionless reduced angular momenta and intensity of the turbulent motions, L_i & σ_i (18 & 23) are the size and velocity dispersion of clouds. The mean values of the reduced angular momenta are found to be independent of z and

$$\langle \mu_1 \rangle = 0.08, \quad \langle \mu_2 \rangle = 0.15, \quad \langle \mu_3 \rangle = 0.15. \quad (27)$$

The small clouds rotation around the longest axis and exponential shapes of PDFs

$$P(x_i) \approx 0.12 \exp(-x_i), \quad x_i = \mu_i / \langle \mu_i \rangle, \quad (28)$$

are consistent with the TTT predictions.

The mean values of the reduced intensity of turbulent motions are also found to be independent of z and

$$\langle \tau_1 \rangle = 0.64, \quad \langle \tau_2 \rangle = 0.76, \quad \langle \tau_3 \rangle = 0.65, \quad (29)$$

and their PDFs are fitted by the functions

$$P(x_i) \approx 0.14 \exp[-(x_i - 1)^2 / 0.14], \quad x_i = \tau_i / \langle \tau_i \rangle. \quad (30)$$

For the total momentum of the clouds, J , and for the total intensity of turbulent motions, j ,

$$J = \sqrt{J_1^2 + J_2^2 + J_3^2} = \mu g_t, \quad j = \sqrt{j_1^2 + j_2^2 + j_3^2} = \tau g_t, \quad (31)$$

$$g_t^2 = (L_1^2 + L_2^2 + L_3^2)(\sigma_1^2 + \sigma_2^2 + \sigma_3^2),$$

we get

$$\langle \mu \rangle = 0.17, \quad \langle \tau \rangle = 0.8. \quad (32)$$

The PDFs for the functions μ & τ are plotted in Fig. 3. The obtained value of $\langle \tau \rangle$ corresponds to domination of elliptical trajectories of particles with the ratio of axes $b/a \approx 0.57$, what is consistent with the ratios of the cloud sizes (18).

For the simulation S_{50} we have, at $1 \leq z \leq 6$ and for the same mass range, instead of (27), (29) and (32):

$$\langle \mu_1 \rangle = 0.08(1 - 0.07z), \quad \langle \tau_1 \rangle = 0.57,$$

$$\langle \mu_2 \rangle = 0.1(1 - 0.07z), \quad \langle \tau_2 \rangle = 0.60(1 - 0.08z), \quad (33)$$

$$\langle \mu_3 \rangle = 0.09(1 - 0.1z), \quad \langle \tau_3 \rangle = 0.57(1 - 0.09z),$$

$$\langle \mu \rangle = 0.13(1 - 0.08z), \quad \langle \tau \rangle = 0.7(1 - 0.08z).$$

Comparison of $\langle \mu \rangle$ with $\langle \tau \rangle$ in (27), (29), (32) and (33) shows that only $\sim 15 - 20\%$ of the angular momenta of individual particles are transformed into the angular momentum of a cloud as a whole, what characterizes the efficiency of the generation of angular momentum according to the TTT.

These results are also consistent with predictions of the Zel'dovich theory (4 – 7) and indicate the significant contribution of initial random velocities in the turbulent motions within compressed clouds.

3.4 Relaxation of the compressed matter

The three parameters w_1, w_2 & w_3 introduced in (8) allow us to discriminate between the regular expansion and compression of matter along the principal axes and to estimate the degree of matter relaxation. As noted in Sec. 2.2, $w_i \geq 1$ indicates domination of matter expansion, while $w_i \leq 1$ corresponds to domination of matter compression along the i^{th} principal axis. For the simulation S_{150} and for redshifts $z = 1, 2, 3$ the mean values $\langle w_i \rangle$ are listed in Table 1 and

Table 1. Degree of relaxation of selected clouds

	$z=1$	$z=2$	$z=3$
$\langle w_1 \rangle - 1$	0.05	-0.2	-0.42
$\langle w_2 \rangle - 1$	-0.4	-0.53	-0.62
$\langle w_3 \rangle - 1$	-0.2	-0.42	-0.55
f_{rel}	0.8	0.44	0.2

their PDFs are plotted in Fig. 4. These results indicate that for our samples of selected clouds the matter compression along all three axes dominates but it is progressively decelerated with time. The symmetry of the PDF $P(w_1)$ points out that for our selected clouds both the compression and expansion along the longest axis are almost equally typical. These estimates only weakly depend upon the richness of clouds.

Another manifestation of the retained expansion along the longest axis is the tight correlation of velocity dispersion and size:

$$\sigma_1 \propto L_1^{0.8},$$

with the deviation of $\sim 10\%$. This expression is quite similar to the Hubble flow. For the middle and the shortest axes such correlations are very weak.

These results confirm that along the longest principal axis the relatively slow relaxation is accompanied by the retained expansion of clouds, which persists for some time after cloud formation. In contrast, along the middle and shortest principal axes the moderate retained compression of clouds predominates. These results are consistent with the strongest matter compression along the shortest principal axis (which is responsible for pancakes formation) and the successive transformation of prolate pancake – like clouds into elongated filamentary – like ones.

To estimate the degree of matter relaxation along the shorter axis we can use the fraction of clouds, $f_{rel}(z)$, for which $|1 - w_3(z)| \leq 0.5$. For three redshifts the estimates of this fraction are listed in Table 1. The rapid growth of this fraction with time illustrates the progressive relaxation of the compressed matter along the shortest principal axis. The fraction of matter relaxed along the longest principal axis is only half of that along the other two axes. For the simulation S_{500} the functions $\langle w_i(z) \rangle - 1$ and $f_r(z)$ are similar to the ones discussed above.

More complex internal structure of clouds selected from the high resolution simulation S_{50} leads to a more rapid relaxation of the compressed matter. Thus, we have for the matter fraction with $|1 - w_3| \leq 0.5$

$$f_{rel}(z=5) \approx 0.6, \quad f_{rel}(z=3) \rightarrow 0.9. \quad (34)$$

These results illustrate the impact of small scale perturbations and strong links between the resolution achieved in the simulation and the processes of clouds formation and relaxation.

3.5 Colder and hotter clouds

The strong link between the velocity dispersions and richness of clouds (23) illustrates the large scale correlation of the initial velocity field. None the less, the scatter around

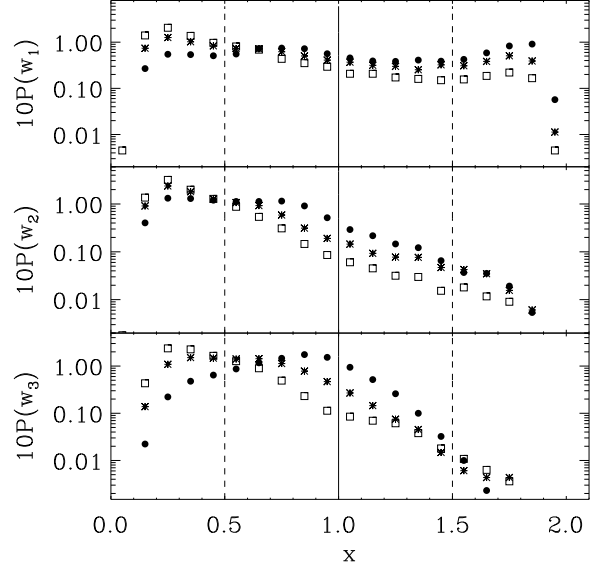


Figure 4. For the simulation S_{150} the PDFs of the ratio of projected velocity and velocity dispersion along the longest, w_1 , middle, w_2 , and shortest w_3 , axes (top, middle and bottom panels) are plotted for redshifts $z = 1, 2 \& 3$ (points, stars and squares) for clouds selected with the threshold overdensity $\delta = 1.76$ and richness given by (3)

the mean dispersions (23) is large and differences between properties of colder and hotter clouds deserve special investigation.

In the simulation S_{150} the subpopulation of colder clouds was selected from the full sample of clouds by the condition that $\sigma_3 \leq 40 \text{ km/s}$. It contains about half of clouds with the lower richness and the steeper mass function $P_c(M_{cl}/\langle M_{cl} \rangle)$:

$$\langle M_{cl}(z) \rangle \approx 7 \cdot 10^{11} h^{-1} M_\odot, \quad P_c(M_{cl}) \propto [M_{cl}/\langle M_{cl} \rangle]^{-2.7}. \quad (35)$$

The subpopulation of hot rich clouds with $\sigma_3 \geq 40 \text{ km/s}$, is characterized by larger mean richness and shallower mass function, $P_h(M_{cl}(z)/\langle M_{cl}(z) \rangle)$,

$$\langle M_{cl}(z) \rangle \approx 3.2 \cdot 10^{12} h^{-1} M_\odot, \quad P_h(M_{cl}) \propto [M_{cl}/\langle M_{cl} \rangle]^{-1.8}. \quad (36)$$

Both colder and hotter subpopulations are dominated by partly relaxed clouds expanded along the longest principal axis and compressed along the middle and shortest axes and for them the numerical estimates of $\langle w_i \rangle$ are quite similar to the ones listed in Table 1. For the subpopulations of hotter clouds the fraction of relaxed clouds with $|1 - w_3(z)| \leq 0.5$ is close to f_{rel} listed in Table 1, while for the colder clouds this fraction is smaller by a half.

4 CORE-SAMPLING APPROACH.

For a more detailed comparison of the simulated matter distribution with the observed characteristics of the LSS and the Ly- α forest it is convenient to use the core-sampling approach (Doroshkevich et al. 2001, 2004; Demiański et al. 2006). With this approach we retain only particles within the selected sample of clouds, and divide the simulated box into a system of rectangular cores of comoving size

$d_{core} \times d_{core} \times L_{box}$, and consider properties of particles situated within each core.

All particles within a core are projected on the core axis and using the 1D cluster analysis are collected into clumps. For so selected clumps we can determine several characteristics such as the mass, M_{cr} , and the comoving surface density, $q_{cr} = M_{cr}/d_{core}^2$. Other characteristics relate to the clump position and velocity along the core. They are the comoving clump separation, D_{sep} , and their size (thickness), t_{cr} , and overdensity, $\delta_{cr} = q_{cr}/t_{cr}/\langle\rho\rangle$, the relative velocity of neighbouring clumps, $|\delta U|$, the dispersions of clump velocity, σ_U , and particle velocity within clumps, σ_v . We can also estimate the degree of matter relaxation, w_{cr} , (8), and the dispersion of transverse velocity of matter within clumps, σ_{tr} .

The core-sampling analysis utilizes four parameters, namely, the comoving size of the core, d_{core} , the comoving threshold linking length used in the 1D cluster analysis, l_{thr} , and the minimal and maximal richness of clumps, q_{thr} & q_{max} , retained for the analysis. Results of the analysis depend mainly upon the choice of d_{core} . Two last parameters allow us to remove from the sample poor clumps that arise owing to random intersection of the core and a cloud periphery, and small number of extremely rich clumps with $q \geq q_{max}$, what strongly distorts the mean measured characteristics.

Here we apply the core-sampling approach to investigate the full sample of clouds selected in the simulation S_{150} with the threshold overdensity $\delta_{thr} = 1.76$. In our analysis, we use

$$d_{core} = 1.5 h^{-1} \text{Mpc}, \quad l_{thr} = 0.5 h^{-1} \text{Mpc}, \quad (37)$$

$$q_{thr} = M_{cs}/d_{core}^2 = 3 \cdot 10^{11} M_{\odot} h \text{Mpc}^{-2}, \quad q_{max} = 10 q_{thr}.$$

These samples contain $\sim (1.3 - 1.5) \cdot 10^5$ clumps. Naturally, variations of these parameters change the fraction of low and high mass clumps in the selected sample and also the main characteristics of the sample of clumps. However for a wide set of limits (37) we see a weak redshift dependence of the mean characteristics and their PDFs, what confirms the self similar character of the LSS evolution.

In many respect this approach and its limitations are similar to those appearing in the analysis of the Ly- α forest (Demiański et al. 2006) and the pencil beam observations of the LSS (Doroshkevich et al. 2001, 2004). Of course the criteria of clump selection in observations and simulations are not identical. Indeed, if the Doppler parameter of the forest line coincides with the velocity dispersion σ_v , then the evolutions of the DM surface density $q(z)$ and the column density of neutral hydrogen, N_{HI} , are very different as they are driven by different factors. Thus, we cannot directly compare simulated results with observations. However even such analysis allows us to reveal qualitative similarity of the observed and simulated LSS evolution and to demonstrate the impact of the main factors that influence evolution of the observed LSS.

4.1 Dynamical characteristics of the DM LSS

The redshift evolution of dynamical characteristics of the simulated DM clumps obtained with the core sampling approach are found to be similar to those obtained in the pre-

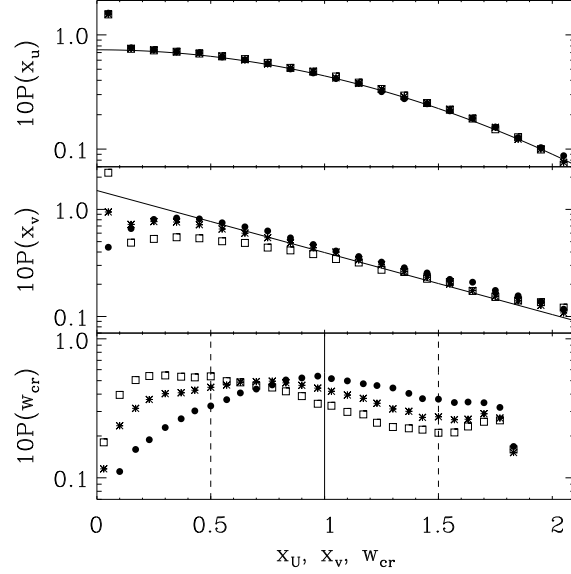


Figure 5. The PDFs of clusters velocity, $P(x_u)$, the velocity dispersion within clusters, $P(x_v)$, and the degree of relaxation, $P(w_{cr})$, are plotted for redshifts $z = 1, 2$ & 3 (points, stars and squares) for clusters selected within cores under conditions (37). Here $x_u = |U|/\sigma_U$, $x_v = \sigma_v/\langle\sigma_v\rangle$.

vious section. Thus, with the threshold parameters (37) and for $3 \geq z \geq 1$ we get for the velocity dispersion of clumps, σ_U , and for the relative velocity of neighboring clumps, δU

$$\langle\sigma_U\rangle \approx 308 \text{km/s} (1+z)^{-1/2} (1 \pm 0.05), \quad (38)$$

$$\langle|\delta U|\rangle \approx 272 \text{km/s} (1+z)^{-1/2} (1 \pm 0.03). \quad (39)$$

So defined σ_U and the value (11) measured for all particles are close to each other. The PDF for the dispersion of the 1D clumps velocity, $P(x_u = |U|/\sigma_U)$, plotted in Fig. 5 (top panel) is close to the Gaussian one. However at all redshifts there is some excess of clumps ($\sim 6\%$) with extremely low σ_U .

Both velocity dispersions of the compressed matter measured with the core sampling approach along the core, $\langle\sigma_v\rangle$, and in the transverse directions, $\langle\sigma_{tr}\rangle$, are weakly dependent upon redshift, what is similar to the behavior of the σ_i (23). Thus we get

$$\langle\sigma_v\rangle \approx \langle\sigma_{tr}\rangle \approx 49 \text{km/s} (1 \pm 0.2). \quad (40)$$

The random orientation of the cloud principal axes and the probing core leads to intermixture of velocities along three principal axes, and the velocity dispersion measured in transverse directions, $\langle\sigma_{tr}\rangle$, is the same as $\langle\sigma_v\rangle$ measured along the core.

The PDFs of the velocity dispersion of matter compressed within clumps, $P(x_v = \sigma_v/\langle\sigma_v\rangle)$, is plotted in Fig. 5 (middle panel) for three redshifts, $z = 1, 2, 3$. As is seen from this Figure for $x_v \geq 0.5$ these PDFs are quite similar to each other and they are well fitted by the exponential function

$$P(x_v) \approx 1.5 \exp(-x_v/0.75). \quad (41)$$

However fraction of clumps with $x_v \leq 0.1$ progressively decreases with time from $\sim 25\%$ at $z=3$ and down to 10%

at redshifts $z = 1$. This fraction can be related to the low mass unrelaxed clumps formed due to the intersection of cores with complex low density periphery of the selected 3D clusters.

As before, the mean value $\langle w_{cr} \rangle \approx 1$ characterizes the symmetry of the matter compression and expansion along the core in the sample of selected clumps. However, the PDF $P(w_{cr})$ plotted in Fig. 5 (bottom panel) characterizing the degree of matter relaxation along the core shows some variation with redshift. Using this PDF we can estimate the fraction of clumps, $f_{rel}(z)$ with $0.5 \leq w_{cr} \leq 1.5$ which are almost relaxed along the core at redshifts $z = 3, 2$, & 1 as follows:

$$f_{rel}(3) = 0.56, \quad f_{rel}(2) = 0.64, \quad f_{rel}(1) = 0.7. \quad (42)$$

These fractions are similar to the fraction of clusters relaxed along the shortest axis listed in Table 1, what demonstrates moderate impact of the macroscopic motions along the core. This result seems to be natural because of the moderate difference between the fraction of matter relaxed along the shortest and longest principal axes (Table 1 & Fig. 4).

4.2 Spatial characteristics of the DM LSS

The simulated overdensity of clumps, $\langle \delta_{cr} \rangle$, the surface density, $\langle q_{cr}(1+z)^{-2} \rangle$, and the comoving thickness of clusters, $\langle t_{cr} \rangle$, are found to be weakly dependent upon the redshift,

$$\langle q_{cr}(1+z)^{-2} \rangle \approx 4 \cdot 10^{11} \frac{h M_{\odot}}{Mpc^2} (1 \pm 0.2),$$

$$\langle t_{cr} \rangle \approx 1 \, h^{-1} \text{Mpc} (1 \pm 0.1), \quad (43)$$

$$\langle \delta_{cr} \rangle = \left\langle \frac{q_{cr}}{t_{cr} \langle \rho \rangle (1+z)^2} \right\rangle \approx 5 (1 \pm 0.15),$$

where $\langle \rho \rangle$ is the mean comoving density (1).

The redshift evolution of the comoving cluster separation,

$$\langle D_{sep} \rangle \approx 16.2 h^{-1} \text{Mpc} (1 \pm 0.1), \quad (44)$$

is also weakly dependent upon redshift but it strongly depends upon threshold parameters (37) determining the clumps selection procedure.

For the simulation S_{50} the mean comoving separation between clumps is

$$\langle D_{sep} \rangle \approx 7 h^{-1} \text{Mpc}. \quad (45)$$

The difference between this value and (44) illustrates the impact of the box size (the limited core length). The same result as (45) is obtained when we cut a “box” of $50 h^{-1} \text{Mpc}$ from the simulation S_{150} .

The PDFs of the DM surface density, $P(q_{cr}/\langle q_{cr} \rangle)$, and of the objects separation, $P(D_{sep}/\langle D_{sep} \rangle)$, also weakly depend on redshift and are well fitted by exponential functions

$$P(x_q) \approx 0.8 \exp(-x_q/0.8), \quad x_q = q_{cr}/\langle q_{cr} \rangle \geq 0.2, \quad (46)$$

$$P(x_{sep}) \approx 0.9 \exp(-x_{sep}), \quad x_{sep} = D_{sep}/\langle D_{sep} \rangle.$$

These results show that with the core-sampling approach the redshift evolution of the simulated LSS is well characterized by the slow regular variations of its mean characteristics, while the corresponding PDFs practically

do not change at all. This fact verifies again the self similar character of the LSS evolution, at least for its richer elements formed by the DM component of the Universe. It is consistent with the observed evolution of the Ly- α forest (Demiański et al. 2006).

5 SUMMARY AND DISCUSSION

Many branches and strongly nonhomogeneous matter distribution typical for the richer LSS elements determine their complex multiconnected structure and do not allow to characterize them in any simple way. Thus, we are compelled to restrict our analysis to the sample of compact DM clouds with a moderate richness and overdensity. The simple procedure of the sample selection and the basic characteristics of clouds are described in Sec. 2. More refined technique proposed for selection and discrimination of the DM filaments and walls (see, e.g., discussion in Doroshkevich et al. 2004, Aragon-Calvo et al. 2007; Zhang et al. 2009) can be efficient mainly for the solution of some special problems.

In many respects evolution of the selected population is typical for all LSS elements but some discussed characteristics depend upon the procedure of sample selection. First of all this relates to the spatial characteristics of clouds.

As is well known the LSS evolution is determined by the accretion of diffuse matter, creation of poorer clouds and integration of clouds into larger ones. These processes lead to rapid matter concentration within population of large multiconnected clouds and to successive network formation. Thus, in the simulation S_{150} the matter fraction accumulated by richer clouds with $M_{cl} \geq 10^{14} h^{-1} M_{\odot}$ increases by a factor of 5 between redshifts $z = 3$ and $z = 0$, while the fraction of particles accumulated by clouds with $5 \cdot 10^{11} h^{-1} M_{\odot} \leq N_p \leq 10^{14} h^{-1} M_{\odot}$ increases by a factor of 1.5 only. This means that at $z \leq 3$ the LSS evolution is dominated by successive integration of the earlier formed LSS elements into the richest ones. The evolution of compact clouds with moderate richness is determined by a balanced action of coalescence and formation of new clouds.

The existence of the population of DM clouds with moderate richness is in itself quite interesting. In many respects its slow evolution leads to the stability of measured clouds characteristics, which are distorted mainly by the successive formation of high density cores. However, at higher redshifts the influence of the process of integration of clouds becomes less significant, the creation of new clouds and accretion of diffuse matter dominate and characteristics of clouds (21) evolve more rapidly.

The performed analysis of the simulated DM LSS allows us to clarify some important factors that cause its evolution, and to link them with the power spectrum of the initial perturbations and with the observed evolution of the Ly- α forest. The limited mass resolution – $M \sim 2 \cdot 10^{10} M_{\odot}$ and $M \sim 7 \cdot 10^7 M_{\odot}$ in analyzed simulations – prevents the formation of low mass clouds comparable with the majority of the observed Ly- α absorbers. This means that our results cannot be directly compared with the observed characteristics of the Ly- α forest. However, such analysis allows us to find some characteristics of evolution of the simulated DM LSS elements, what is very interesting in itself. It is important also that the main basic features of this evolution are

similar in many respects to the observed properties of the Ly- α forest, what allows us to explain some peculiarities of the forest evolution discussed in the Introduction.

5.1 Main inferences

The most important features of the evolution of the selected DM LSS elements can be summarized as follows:

- (i) Weak redshift variations of the basic characteristics of the selected sample of DM clouds such as their mean comoving size and velocity dispersion.
- (ii) Measured PDFs of the basic characteristics of the LSS elements are weakly dependent upon the redshift, what implies the self similar character of the LSS evolution.
- (iii) Significant degree of relaxation of the compressed matter along the shortest principal axis and retained matter expansion along the longest principal axis.
- (iv) Weaker rotation of clouds along their longest axis.
- (v) Some measured clouds characteristics depend on the procedure of clouds selection.

5.2 Impact of simulation parameters

Comparison of characteristics of clouds obtained for three simulations with different box sizes and resolutions shows that some of them are sensitive to the resolution, the box size and the impact of baryonic component. In particular, complex internal structure of clouds selected in the high resolution simulation S_{50} leads to more complex evolution of the basic characteristics of clouds as compared with the results obtained for lower resolution simulations. In the simulation S_{50} clouds are partially fragmented into high density cores, what distorts their dynamical properties. The fraction of high-density virialized clumps increases with resolution achieved in simulation. However, even a large mass fraction (up to 40%) of these high-density clumps does not affect strongly the main qualitative inferences: the self-similar evolution of characteristics of clouds and exponential decline of their PDFs.

The most prominent impact of resolution is detected on the clouds size along the middle and the shortest axes $\ell_{2,3}$ (21), the velocity dispersion along the longest principal axis (25), and the relaxation parameter, while other properties of clouds are quite similar in all three simulations.

In the simulation S_{50} the box size affects separation between clouds (44, 45). The box size of $150 h^{-1}$ Mpc should be enough for the stable reproduction of both these properties.

5.3 Self similarity of the DM LSS evolution

The most interesting result of our analysis is the self similar character of evolution of the DM LSS which is manifested at $z \leq 4 - 5$ as the surprising stability of PDFs of the basic characteristics of clouds found with both the 3D analysis in Sec. 3 and with the core-sampling approach in Sec. 4. This result is obtained for three simulations performed in different way and with different number of particles, resolution and realization of the initial particle positions and velocities. These features are similar also to the redshift independence of PDFs of the observed characteristics of the

Ly- α forest (Demiański et al. 2006). These analogies point to the universal character of the detected self similarity.

Other manifestation of this self similarity is the universality of the NFW density profiles within simulated DM halos (see, e.g., Navarro, Frenk, White 1995, 1996, 1997). The self similar character of the DM halos formation is seen as the regular redshift variations of the internal structure of individual halos. However, the complex process of formation and relaxation of the high density LSS elements and halos can be described analytically as a self similar process only for the simplest cases (see, e.g., Fillmore & Goldreich, 1984; Gurevich, & Zybin, 1995; Sikivie, Tkachev, Wang Yun, 1997; Nusser, 2001).

For objects formed in the course of mildly nonlinear compression the self similar character of evolution is predicted by the Zel'dovich approximation (Zel'dovich 1970; Shandarin & Zel'dovich 1989), where the evolution is described by a product of time and space dependent functions. The statistical description of the DM LSS based on the Zel'dovich theory (Demiański & Doroshkevich 1999, 2004) clearly demonstrates the expected self similarity.

The simulated evolution of DM clouds is a strongly deterministic process driven mostly by the used realization of initial perturbations. The statistical properties of clouds are determined by the correlation and structure functions expressed through the simulated power spectrum. Therefore we can expect that the self similarity of the simulated evolution is caused by the properties of the power spectrum responsible, in particular, for the formation of clouds.

Such self similarity naturally appears for the power spectrum approximated by a power law. Indeed, in this case all correlation and structure functions are described by the time dependent amplitudes and standard space dependent functions. This usually leads to the self similar evolution of the basic statistical characteristics of the DM LSS. The power spectra used in considered here simulations are well approximated by a power law, what explains the found self similarity.

Of course, this inference is related to the limited range of scales of the power spectrum and therefore to the limited range of clouds richness. However, we can expect that this range extends down to the scales typical for the majority of the forest elements, what in turn explains weak redshift variations of the observed PDFs of forest characteristics. In contrast, the more complex process of formation of the largest clouds and the network of the high density LSS elements is driven by the large scale part of the power spectrum that determines the formation of low density bridges between high density clouds. It is convenient to analyze these mildly nonlinear processes on the basis of the Zel'dovich approximation (Demiański & Doroshkevich 1999, 2004).

5.4 Evolution of the velocity dispersions and the degree of relaxation of clouds

Second important result of our analysis relates to the evolution of the internal structure of clouds. Both the moderate mass resolution achieved in simulations and moderate richness of the dominant population of clouds prevents more detailed description of the anisotropic matter distribution within clouds. However, high force resolution achieved in the considered here simulations allows us to estimate, with

a reasonable precision, the evolution of the velocity dispersion and the degree of relaxation of the compressed matter.

The mean values of the velocity dispersions σ_1, σ_2 & σ_3 , (23) and even their PDFs presented in Fig. 2 for three redshifts are quite similar to each other. However, the PDFs of the degree of relaxation presented in Fig. 4 demonstrate significant differences in characteristics of the velocity components. Indeed, at all redshifts the excess of larger values of $w_1 \geq 1$ indicates noticeable contribution of the retained matter expansion and moderate degree of relaxation along the longest axis. At the same time, the excess of smaller values of $w_2 \leq 1$ demonstrates domination of matter compression along the middle axis and progressive transformation of a pancake like cloud into a filamentary like one. The degree of relaxation along this axis is moderate but it is larger than that along the longest axis.

In contrast, the more symmetric shape of the PDF $P(w_3)$ in Fig. 4 indicates that similar fraction of matter is expanded and compressed along the shortest axis. This Figure shows progressive point concentration near the center, what reflects the progressive randomization of velocities and growth of the degree of relaxation of the compressed matter. Evaluation of the fraction of relaxed clouds and the corresponding matter fraction f_{rel} (Table 1) characterizes these processes quantitatively.

Similar characteristics of the velocity dispersions are also obtained with the simulations S_{500} and S_{50} . The most serious quantitative divergences are found for characteristics of low mass clouds and are discussed in Sec. 3.

It is interesting, that the estimated state of relaxation of clouds with the core sampling approach in (42) is very close to that obtained with the 3D analysis. This fact shows that the random orientation of the clouds with respect to the line of sight results in the intermixture of thermal and large scale bulk velocities but does not distort strongly the measured velocity dispersions and the degree of relaxation of compressed matter.

Special analysis confirms that the subpopulations of colder and hotter clouds with $\sigma_3 \leq \langle \sigma_3 \rangle$ and $\sigma_3 \geq \langle \sigma_3 \rangle$ respectively, contain comparable fractions of matter with different mean richness and mass functions. Both subpopulations are dominated by partly relaxed clouds slowly expanding along the longest principal axis. The colder clouds represent population of anisotropic low mass clouds and both the shape of their mass function and PDFs of other characteristics are strongly depended upon parameters used for selection of the considered DM clouds. In contrast, for population of richer clouds the PDFs of cloud characteristics only weakly depend on the parameters that select these clouds.

A strong difference between velocity dispersions σ_U (9) and σ_i (23) related to the motion of clouds as a whole and to velocities within clouds is caused by the large scale spatial modulation of the initial velocity field in regions of the clouds formation. The same effect is seen in estimates of the relative velocities of neighboring clusters, ΔU (39).

5.5 Angular momentum of the LSS elements.

Recently the angular momenta of the LSS elements are widely discussed and compared with the alignments and angular momenta of galaxies and their DM halos (see, e.g., Vitvitska et al. 2002; Patiri et al. 2006; Lee & Erdogdu 2007;

Park et al. 2007; Aragon-Calvo et al. 2007, 2008; Cuesta et al. 2008; Paz et al. 2008; Slosar et al. 2009; Jimenes et al. 2009; Zhang et al. 2009; Lovell et al. 2010). The main inferences of the TTT and, in particular, preferential orientation of the angular momenta along the shortest axes of the LSS elements are basically confirmed. Influence of the anisotropic matter infall into the LSS elements on their angular momenta was discussed by Doroshkevich (1973) for baryonic component and in Bernardo et al. (2002) for DM particles. However, analysis of simulations shows that for DM component contribution of this effect is moderate and our results obtained in Sec. 3.4 are consistent with TTT predictions.

On the other hand, large scatter is found between the shape of the host LSS element and the angular momenta of galaxies and their DM halos incorporated in that element. This scatter is expected and can be caused by action of several factors.

Thus, comparison of the functions J & j (31) shows that the process of generation of angular momentum of DM clouds is only moderately efficient (less than 20%). This fact in itself suggests a weak correlation between the angular momenta of the host LSS element and high density low mass subclouds and it basically explains the scatter mentioned above. Moreover, more detailed analysis of the process of halo formation (Vitvitska et al. 2002) shows strong evolution of the angular momentum of DM halos and its dependence upon the angular momenta of merged satellites. Perhaps, stronger correlation can be found between properties of the host cloud and the system of DM halos and its satellites.

Let us note also that this scatter is partly enhanced by uncertainties in the determination of the complex shapes of the LSS elements. This is specially important for observations when the shape of such elements can be found only approximately.

5.6 The DM LSS elements and the Ly- α forest.

The main observed characteristics of the Ly- α forest were analyzed in many publications (see, e.g. Demiański et al. 2006 and references there). Detailed discussion of the observed characteristics of the Ly- α absorbers can be found, for example, in Kim, Cristiani & D’Odorico (2002), Kim et al. (2002, 2004).

There are some essential differences between the sample of simulated DM clouds and the observed Ly- α absorbers. The most important of them are:

- (i) The Ly- α forest is related with the LSS elements with sizes, masses and other parameters much smaller than the simulated ones.
- (ii) The Ly- α forest is observed for larger neutral hydrogen column density, $N_{HI} \geq 10^{12} \text{ cm}^{-2}$, which depends upon the UV background and is not directly linked with the DM component of absorbers.
- (iii) The evolution of the observed Ly- α absorbers depends upon the poorly known UV background and can significantly differ from the evolution of the simulated DM LSS.

These differences prevent a direct quantitative comparison of characteristics of the simulated DM LSS and the observed Ly- α forest. However, the absorbers are dominated by the DM component, and, so, qualitative comparison of

their properties and evolution with the simulated one allows us to clarify some problems of the forest evolution.

First of all the self similar character of evolution of the Doppler parameter, b , is reflected in the surprising stability of its PDFs (Demiański et al. 2006). The b parameter strongly depends upon the DM component and we can expect that the most important aspects of its evolutions are closely correlated with the characteristics of evolution of DM clouds.

The weak redshift dependence of the Doppler parameter and the high degree of matter relaxation along the line of sight for majority of the Ly- α absorbers are consistent with results obtained in Sec. 3.3, 3.5 and 4.1. It is important also, that the complex shape of the PDF $P(b)$ is quite similar to the PDF $P(\sigma_3)$ plotted in Fig. 2.

Our analysis in Sec. 4.2 cannot reproduce criteria of the Ly- α forest selection and in particular the redshift evolution of clumps separation (44, 45) does not represent the evolution of linear number density of the forest elements. The most important among the unknown factors are the disintegration of richer forest elements into a system of high density subclouds linked by extended low density bridges, and variations of the ionizing UV background. Comparison of the LSS evolution in simulations S_{150} and S_{50} confirms that the small scale perturbations accelerate the disintegration of the LSS elements and their internal structure becomes more complex. These problems need to be studied in more details with more representative and high resolution simulations.

Acknowledgments

We wish to thank Dr. E. Tittley for many useful comments and suggestions on this paper. This paper was supported in part by the Russian Fund of Fundamental Investigations grant Nr. 08-02-00159 & 09-02-12163, Federal Program "Scientific and Pedagogical Personal Innovative of Russia" Nr. 1336 and Polish Ministry of Science and Higher Education grant NN202-091839.

REFERENCES

- Abazajian K., et al., 2003, *AJ*, 126, 2081
 Aragon-Calvo M., van de Weygaert R., Jones B., van der Hulst J., 2007, *ApJ*, 655, L5
 Aragon-Calvo M., Platen E., van de Weygaert R., Szalay A., 2008, *astro-ph/0809.5104*
 Bernardo F., Colombi S., Gaztanaga E., Scoccimarro R., 2002, *Physics Reports*, 367, 1
 Bullock J.S., Dekel A., Kolatt T.S., Kravtsov A., Klypin A., Porciani C., & Primack J., 2001, *ApJ*, 555, 240
 Croft R.A.C. et al., 2001, *ApJ*, 557, 67
 Croft R.A.C. et al., 2002, *ApJ*, 581, 20
 Cuesta A., Betancort-Rijo J., Gottlöber S., Patiri S., Yepes G., Prada F., 2008, *MNRAS*, 385, 867
 Davé R., Hernquist L., Katz N., Weinberg D.H., 1999, *ApJ*, 511, 521
 Davis M. et al., 2003, *Proc. SPIE*, 4834, 161
 Demiański M. & Doroshkevich A., 1999, *MNRAS*, 306, 779
 Demiański M. & Doroshkevich A.G., 2003, *ApJ*, 597, 81
 Demiański M. & Doroshkevich A., 2004, *A&A*, 422, 423
 Demiański M. & Doroshkevich A., & Turchaninov V.I., 2006, *MNRAS*, 371, 915
 Diemand J., Kuhlen M., Madau P., Zemp M., Moore B., Potter D., Stadel J., 2008, *Nature*, 454, 735
 Doroshkevich, A.G., 1970, *Astrofizika*, 6, 581
 Doroshkevich, A.G., 1973, *Soviet Astronomy*, 16, 986
 Doroshkevich, A.G., Tucker, D.L., Fong R., Turchaninov V., Lin H., 2001, *MNRAS*, 322, 369
 Doroshkevich, A.G., Tucker, D.L., Allam S. & Way M., 2004, *AA*, 418, 7
 Fillmore J.A., & Goldreich P., 1984, *ApJ*, 281, 1
 Frenk C.S., 2002, *Philos.Trans.R.Soc. London*, 300, 1277
 Gnedin N.Y. & Hamilton A.J.S., 2002, *MNRAS*, 334, 107
 Gottlöber S., Yepes Y., 2007, *ApJ*, 664, 117
 Gurevich A.V., & Zybin K.P., 1995, *Physics-Uspekhi*, 38, 687
 Jimenez R., et al., 2010, *MNRAS*, 404, 975
 Kim T.S., Cristiani S., & D'Odorico S., 2002, *A&A*, 383, 747
 Kim T.S., Carswell R.F., Cristiani S., D'Odorico S. & Giallongo E., 2002, *MNRAS*, 335, 555
 Kim T.S., Viel M., Haehnelt M., Carswell R.F., Cristiani S., 2004, *MNRAS*, 347, 355
 Kravtsov, A., Klypin, A., Khokhlov, A., 1997, *ApJS*, 111, 73
 Le Fevre O. et al., 2005, *AA*, 439, 845
 Lee J., Erdogdu P., 2007, *ApJ*, 671, 1248
 Lovell, M., Eke V., Frenk C., Jenkins A., *arXiv:1008.0484*
 Manning C., 2003a, *ApJ*, 591, 79
 Manning C., 2003b, *ApJ*, 595, 19
 McDonald P. et al., 2005, *ApJ*, 635, 761
 McLin K., Stocke J.T., Weymann R., Penton S.V., Shull M., 2002, *ApJ*, 574, L115
 Meiksin A., Bryan G., Machacek M., 2001, *MNRAS*, 327, 296
 Morris S., Weimann R.J., Savage B.D., Gilland R.L., 1993, *ApJ*, 377, L21
 Morris S., Weimann R.J., Dressler A., McCarthy P.J., 1993, *ApJ*, 419, 524
 Navarro J.F., Frenk C.S., & White S.D.M., 1995, *MNRAS*, 275, 720
 Navarro J.F., Frenk C.S., & White S.D.M., 1996, *ApJ*, 462, 563
 Navarro J.F., Frenk C.S., & White S.D.M., 1997, *ApJ*, 490, 493
 Nusser A. 2001, *MNRAS*, 325, 1397
 Panter B., Jimenes R., Heavens A., Charlot S., 2007, *MNRAS*, 378, 1550
 Park C., Choi Y., Vogelry M., Gott III R., Blanton M., 2007, *ApJ*, 658, 898
 Patiri S., Cuesta A., Prada F., Betancort-Rijo J., Klypin A., 2006, *ApJ*, 652, L75
 Paz D., Stasyszyn F., Padilla N., 2008, *MNRAS*, 389, 1127
 Peebles P.J.E., 1969, *ApJ*, 155, 393
 Penton S.V., Shull J.M., & Stocke J.T., 2000, *ApJ*, 544, 150
 Penton S.V., Stocke J.T., & Shull J.M., 2002, *ApJ*, 565, 720
 Percival W. et al., 2001, *MNRAS*, 327, 1297
 Schaye J., 2001, *ApJ*, 559, 507
 Seljak U., McDonald P., Makarov A., 2003, *MNRAS*, 342, L79
 Seljak U. et al., 2005, *Phys. Rev. D*, 71, 103515
 Schäfer B., 2008, *astro-ph/0808.0203*
 Shandarin S., Zel'dovich Ya.B., 1989, *Rev.Mod.Phys.*, 61, 185
 Sikivie P., Tkachev I.I., Wang Yun, 1997, *Phys. Rev.D*, 56, 1863
 Skibba R. et al., 2009, *MNRAS*, 399, 966
 Slosar A. et al., 2009, *MNRAS*, 392, 1225
 Springel V., Frenk C.S., & White S.D.M., 2006, *Nature*, 440, 1137
 Springel V., 2005, *MNRAS*, 364, 1105
 Springel V., et al. 2008, *MNRAS*, 391, 1685
 Tasitsiomi A., Kravtsov A.V., Gottlöber S., Klypin. A., 2004, *ApJ*, 607, 125
 Tegmark M., Zaldarriaga M., 2003, *Phys. Rev. D*, 66, 103508
 Theuns T., Leonard A., Schaye J., Efsthathiou G., 1999, *MNRAS*, 303, L58
 Theuns T., Schaye J., Haehnelt M., 2000, *MNRAS*, 315, 600
 Trujillo I., Carretero C., Patiri S., 2006, *ApJ*, 640, L111
 Verde L., et al., 2003, *ApJS*, 148, 195.

- Viel M., Haehnelt M.G., Carswell R.F., Kim T.-S., 2004a, MNRAS, 349, L33
- Viel M., Haehnelt M.G., Springel V., 2004b, MNRAS, 354, 684
- Vitvitska M., Klypin A., Kravtsov A., Wechsler R., Primack J., Bullock J., 2002, ApJ, 581, 799
- Weinberg D.H., Burles S., Croft R.A.C., et al., 1998, in "Evolution of Large Scale Structure: From Recombination to Garching", eds. A.J. Banday, R.K. Sheth, L.N. Da Costa, p. 346
- White S.D.M., 1984, ApJ, 286, 38
- Williger et al. 2010, MNRAS, 405, 1736
- Wojtak R., Lokas E., Gottlöber S., Mamon G., 2005, MNRAS, 361, L1
- Zel'dovich Ya.B., 1970, Astrophysica, 5, 20
- Zhang Yu., Meiksin A., Anninos P., Norman M.L., 1998, ApJ., 495, 63
- Zhang Y., Yang X., Faltenbacher A., Springel V., Lin W., Wang H., 2009, astro-ph/0906.1654